Seasonal variation in aerosol chemistry drives new particle formation and CCN activity in a coastal city, China: insights from year-long online measurements in Fuzhou

Zihan Wang[1], Yishu Bian[2], Fuwang Zhang[3], Honglei Wang[1*], Wen Lin[2], Jun Hu[4], Tianliang Zhao[1], Lijian Shen[2,5], Zuxin Xie[2]

[1] Collaborative Innovation Center on Forecast and Evaluation of Meteorological Disasters (CIC–FEMD), China Meteorological Administration Aerosol–Cloud and Precipitation Key Laboratory, Nanjing University of Information Science and Technology, Nanjing 210044, China

[2] Fujian Key Laboratory of Severe Weather and Key Laboratory of Straits Severe Weather, China Meteorological Administration, Fuzhou 350001, China

[3] Fujian Provincial Environmental Monitoring Central Station, Fuzhou 350003, China

[4] Fujian Provincial Academy of Environmental Science, Fuzhou 350001, China

[5] Key Laboratory of Ecosystem Carbon Source and Sink, China Meteorological Administration (ECSS-CMA), Wuxi University, Wuxi 214105, China

Correspondence to: Honglei Wang (hongleiwang@nuist.edu.cn)

Abstract: New particle formation (NPF) is an important source of cloud condensation nuclei (CCN), which affects the global climate. Continuous observations in the coastal city of Fuzhou, conducted from June 2021 to May 2022, aimed to study NPF events and their impact on CCN. A total of 46 NPF events were identified, with a frequency of 12.7 %. The average formation rate (FR) and growth rate (GR) of particles were 3.94 ± 8.26 $cm^{-3}·s^{-1}$ and 5.20 ± 1.78 $nm·h^{-1}$. The NPF events showed evident seasonal variation: spring (27.17%), fall (9.89%), winter (8.89%), and summer (4.35%). Spring NPF events were characterized by high FR (5.56 $cm^{-3}·s^{-1}$) and suppressed growth processes, while summer, under the dominance of marine winds, exhibited the lowest FR yet the highest GR among all seasons (peak value 11.68 $nm·h^{-1}$). The influence of NPF on the chemical composition of $PM_{2.5}$ and CCN also showed seasonal differences. In summer, NPF generated substantial amounts of sulfate and nitrate, resulting in stronger particle hygroscopicity (> 0.6). In fall and winter, higher concentrations of black carbon (BC) and primary organic carbon (POC) led to weaker κ_{inorg} (≤0.55). XGBoost-SHAP attribution further quantified that FR is dominated by physical processes (nucleation mode 76.2 %, CS 13.8 %), with a sharp NH_3 threshold at 4 $\mu g\ m^{-3}$ and a narrow temperature range (20–25 °C). For particle growth, temperature shows a linear positive effect above 20°C, and RH > 60 % consistently suppresses particle concentrations.

The enhancement effect of NPF on CCN was most significant in summer (E_N_{CCN} = 1.64), accompanied by CCN growth. In spring, the high condensation sink (CS) suppressed growth, leading to an insignificant CCN enhancement effect. In fall and winter, NPF-induced CCN enhancement mainly occurred 3–5 hours after the event, with increases ranging from 13% to 65%, particularly notable at high supersaturation levels (0.8–1.0% SS).

1 Introduction

New particle formation (NPF) is a complex process in which gaseous precursors in the atmosphere nucleate and condense to form new particles, which subsequently grow through condensation, coagulation, and other processes. NPF contributes over 50 % of the global cloud condensation nuclei (CCN), significantly influencing cloud albedo, structure, lifetime, and solar radiation reaching the Earth's surface (Tröstl et al., 2016; Yao et al., 2018). Additionally, efficient nucleation and explosive growth of particles are important sources of haze formation in urban atmospheres, impacting air quality and public health (Kulmala et al., 2021).

Although its frequency may vary with season and location, NPF events fundamentally represent competition between aerosol particle sources and sinks. Current research indicates that secondary particle formation is driven by the photochemical oxidation of atmospheric gases. Sulfuric acid and highly oxidized molecules can act as nucleation precursors (Fan et al., 2018; Zaveri et al., 2022). Furthermore, ions may also play a role in particle nucleation, though their significance remains debated (Hirsikko et al., 2011; Kirkby et al., 2016). Pre-existing aerosol particles act as a sink for these precursors, small clusters, and newly formed particles, thereby suppressing NPF occurrence (McMurry and Friedlander, 1979). However, frequent NPF events also occur in heavily polluted cities (Sun et al., 2015; Yao et al., 2018). Therefore, the mechanisms governing NPF generation and growth under different atmospheric conditions are still under investigation.

NPF events can be described by the formation rate (FR) of nucleation-mode particles and the growth rate (GR) of newly formed particles (Kulmala et al., 2012). The formation rate of 3 nm particles in the boundary layer typically ranges from 0.01 to 10 $cm^{-3} \cdot s^{-1}$, while the typical growth rate in mid-latitudes ranges from 1 to 20 nm h^{-1} (Kulmala et al., 2004). Yli-Juuti et al. (2011) reported typical growth rates of

1.8–10.7 $nm \cdot h^{-1}$ for 1.5–20 nm particles. Previous studies have shown that NPF is enhanced in the presence of sulfuric acid, alkaline substances, organic acids, and ions (Wang et al., 2011) but suppressed in the presence of nitrogen oxides (NO_x) (Wildt et al., 2014), indicating significant synergistic effects in chemically complex mixtures (Guo et al., 2014). The availability of precursor vapors and the atmospheric chemical environment play decisive roles. H_2SO_4 is a key nucleating species, and its stabilizing co-components, such as ammonia (NH_3) and amines, can dramatically enhance FR (Dunne et al., 2016; Yao et al., 2018; Kirkby et al., 2016). For particle growth, condensation of low-volatility compounds is the dominant process. Sipilä et al. (2010) showed experimentally that early-stage growth is primarily driven by H_2SO_4 condensation.

Additionally, NPF occurrence is constrained by atmospheric temperature and humidity (Yu et al., 2017; Yue and Hamill, 1979). Low temperatures promote nucleation, whereas high temperatures suppress it (Sipilä et al., 2010; Dunne et al., 2016; Yu et al., 2017). Dunne et al. (2016) further showed that at low temperatures, the ion-enhancement effect is weak due to suppressed evaporation of neutral clusters, while at ambient temperatures, ions can increase the nucleation rate by about a factor of 15. Consequently, neglecting temperature dependence leads to a marked overestimation of NPF and CCN concentrations in summer (Yu et al., 2017). Hamed et al. (2011), based on observations at multiple continental sites, found that NPF events predominantly occur at relative humidity below 60% and are rare above 80%. The reason is that high relative humidity reduces ultraviolet radiation, lowering the production of OH and H_2SO_4; meanwhile, hygroscopic growth enhances the condensation sink, thereby suppressing new particle formation.

Aerosol chemical composition also influences aerosol hygroscopicity, altering its critical diameter and thereby affecting CCN activation and cloud formation (Petters and Kreidenweis, 2007; Williamson et al., 2019; Xu et al., 2020). Petters and Kreidenweis (2007) proposed hygroscopicity parameter (κ)is widely used to quantify the water uptake ability and CCN activity of aerosols. Extensive experimental studies have well characterized the κ values of inorganic salts such as ammonium sulfate, ammonium nitrate, and ammonium bisulfate (Liu et al., 2014; Kuang et al., 2020; Cai et al., 2018; Wu et al., 2016). In the accumulation mode (150–1 μm), inorganic species contribute about 90% of the total κ (Liu et al., 2014).

Observations across different environments (e.g., mountain, urban) have shown that NPF events typically lead to a significant increase in N_{CCN} (Kuwata et al., 2008; Yue et al., 2011; Fan et al., 2018). Kuwata et al. (2008) observed a clear increase in N_{CCN} at different supersaturation levels after NPF events on Jeju Island, South Korea. Research in Beijing indicated that NPF events could increase local N_{CCN} by 0.4–6 times (Yue et al., 2011). In polluted environments, additional condensable species, particularly ammonium nitrate and secondary organic aerosols, can accelerate growth and shorten the time needed for freshly formed particles to reach CCN-active sizes (Zhu et al., 2026). However, some studies suggest that an increase in hydrophobic organic components during subsequent particle growth may inhibit CCN generation. Therefore, understanding the role of different components during particle growth is crucial for assessing their subsequent climate effects.

Although NPF research in China is widespread, most studies focus on reporting occurrence frequencies, formation, and growth rates, or are limited to discussing nucleation mechanisms. For instance, NPF event frequencies at sites like Shangdianzi, Mount Tai, and Lin'an in eastern China range from 15% to 29% (Shen et al., 2018). Frequencies in Beijing, Jinan, and Shanghai are approximately 30%, 40%, and 21%, respectively (Jayaratne et al., 2017; Lv et al., 2018; Xiao et al., 2015). Currently, understanding how regional variations in atmospheric oxidants and precursors affect the growth of newly formed particles to CCN sizes, especially the quantification of their CCN efficiency, remains a challenge and frontier in current research (Cai et al., 2018; Kulmala et al., 2021; Rose et al., 2017; Xiao et al., 2015; Yao et al., 2018). Given that Fuzhou is a rapidly developing southeastern coastal city with unique sea-land breeze conditions, a high-temperature and high-humidity environment, and complex pollution emission characteristics, it may have unique NPF mechanisms. However, there is a lack of long-term comprehensive observation or systematically quantified NPF's CCN efficiency in this region. Therefore, this study conducted a one-year comprehensive observation in Fuzhou from June 2021 to May 2022, providing new insights and data support for understanding the CCN efficiency and potential climate relevance of NPF under China's complex atmospheric environment.

2 Data and Methods

2.1 Observation site

Observation data for this study were collected from June 1, 2021, to May 30, 2022, during comprehensive atmospheric environmental observations conducted at the Fujian Provincial Environmental Monitoring Center Station (26.11°N, 119.30°E, altitude 65 m) and the Fuzhou Meteorological Bureau Station (26.05°N, 119.26°E, altitude 18 m). Both stations are located within Fuzhou's urban area, approximately 8 km apart horizontally. The Fujian Provincial Environmental Monitoring Center Station is situated in Gulou District, the central urban area of Fuzhou, surrounded primarily by commercial, residential, and transportation land, representing areas heavily influenced by intense human activities. The Fuzhou Meteorological Bureau Station is located in Cangshan District, southern Fuzhou, approximately 1.5 km east of the Min River. Fuzhou is situated at the Min River estuary and along the East China Sea coast, characterized mainly by plains (average altitude 10–30 m) and a typical East Asian monsoon climate, significantly influenced by sea-land breeze circulation and marine air masses (Hu et al., 2024). Given the short distance (~8 km) and the regional background homogeneity, the local environments of the two sites are not expected to be drastically different, although each is influenced by its specific surroundings (urban vs. riverside). A comparison of air pollutant concentrations between the two sites using nearby national monitoring stations (Table S2).

2.2 Measurement and instrumentation

A CCN counter (CCN-100; DMT, USA) equipped with a continuous flow of 500 cm^3/min and a thermal gradient was used to measure CCN concentrations at five supersaturation (SS) levels. To maintain counting accuracy, the instrument was regularly calibrated for T gradient, flow rate, pressure, SS, and the optical particle counter (OPC) using standard ammonium sulfate according to the method by Rose et al. (2008). Additionally, zero-point determination was performed before and after each observation to minimize instrumental error. During observations, the measurement interval for each SS level was 10 minutes, and a few minutes were required to stabilize after switching SS levels. Therefore, CCN data collected before reaching stable SS were excluded from subsequent analysis. The typical measurement uncertainty of the CCN-100 is approximately ±10% in Table S1.

An online organic carbon/elemental carbon analyzer (Sunset Laboratory semicontinuous OC/EC analyzer, Model-4, Sunset Laboratory Inc., USA) was used to determine organic carbon (OC) and elemental carbon (EC) content in atmospheric particulate matter samples. The instrument provides hourly averaged concentrations. Details of instrument operation can be found in Chang et al. (2017). Based on replicate analyses reported by Zhang et al. (2021), the within-model measurement uncertainties (relative standard deviation) for the Sunset Model-4 are ±3.6% for OC and ±6.8% for EC.

A Wide-Range Particle Spectrometer (WPS-1000, MSP) measured aerosol number size distributions (10-350 nm) with a time resolution of 6 minutes across 96 channels. To align with the 1-hour meteorological data, the 6-minute distributions were arithmetically averaged to hourly particle number size distributions. Instrument details and principles are described in Wang et al. (2014). The typical uncertainty for particle size distribution measurements in this size range is approximately ±10% in Table S1.

Black carbon (BC) mass concentration was measured using an Aethalometer (AE-33, Magee Scientific) with a time resolution of 1 hour. BC data from the 880 nm wavelength (channel 6) were used (Kirchstetter et al., 2004). The measurement uncertainty is approximately ±10% (Table S1).

An online particle chromatograph (MARGA ADI-2080) continuously monitored mass concentrations of soluble aerosol ionic components (SO_4^{2-}, NO_3^-, NH_4^+, Na^+, K^+, Ca^{2+}, Cl^-) and trace gases (NH_3, HNO_2, HNO_3, HCl, SO_2). Sampling, operation, and internal calibration methods followed Du et al. (2011). The instrument provides hourly averaged concentrations. According to an independent verification study (Battelle, 2009), the measurement precision (median absolute relative percent difference between duplicate units) ranges from 5% for SO_2 to 20% for NH_4^+, with data completeness >90% for all major ions.

Meteorological data (including wind speed (WS), wind direction (WD), temperature (T), relative humidity (RH), and precipitation) with a time resolution of 1 h were obtained from the Fuzhou Olympic Sports Center Meteorological Station. Data on conventional air pollutants (O_3, CO, NO_2, $PM_{2.5}$, and PM_{10}) were sourced from the China National Environmental Monitoring Centre's real-time urban air quality release platform (https://quotsoft.net/air/).

2.3 Analysis methods

The growth rate (GR) of new particles was calculated following (Kulmala et al., 2012):

$$GR = \frac{\Delta D_m}{\Delta t} \quad (1)$$

where D_m is the median diameter of the nucleation mode particles, obtained by fitting a log-normal distribution to the particle number size distribution. Statistics of the fitting results (see Supplementary Material) demonstrate that the log-normal distribution represents the observed particle size distributions well, with the majority of fits yielding high coefficients of determination (R^2>0.85); only fits with R^2>0.7 were used to avoid propagating poor-fitting uncertainties. GR describes how rapidly particles grow from the nucleation size to larger sizes. It is later used to estimate the formation rate of new particles (Eq. 2) and condensable vapor concentration (Eq. 4) and to evaluate the competition between condensation and coagulation during NPF events.

The condensation sink (CS) reflects the rate at which condensable vapor molecules condense onto the surface of pre-existing atmospheric particles and was calculated as follows (Kulmala et al., 2012):

$$CS = 4\pi D \sum_i \beta_{M,i} \cdot D_i \cdot N_i \quad (2)$$

where D is the diffusion coefficient of the vapor (typically assumed to be sulfuric acid), N_i is the number concentration of particles in a given size bin, and β_M is a correction factor.

The coagulation sink (CoagS) reflects the ability and rate of pre-existing atmospheric particles to remove newly formed nucleation particles via coagulation. For particles of size i, the coagulation sink can be expressed as:

$$CoagS_i = \sum_j K_{ij} N_j \quad (3)$$

where N_j is the number concentration of particles in size bin j, and K_{ij} is the Brownian coagulation coefficient between particles of size j and i.

The formation rate (FR) of new particles was calculated following Kulmala et al. (2012):

$$FR = \frac{dN_{nuc}}{dt} + CoagS_{nuc} \cdot N_{nuc} + \frac{GR}{\Delta dp} + S_{losses} \quad (4)$$

where N_{nuc} is the number concentration of nucleation-mode particles. Following the definition by Kulmala et al. (2012), the nucleation-mode size range in this study was also limited to below 25 nm. $CoagS_{nuc}N_{nuc}$ is the flux of particles lost due to coagulation with pre-existing particles, where $CoagS_{nuc}$ is the coagulation sink for nucleation-mode particles. $GR/\Delta dp$ represents the flux of particles growing out of the nucleation size range (exceeding 25 nm), which is generally negligible under typical

atmospheric conditions (Dal Maso et al., 2005). FR is later used to compare NPF event intensity under different meteorological and chemical conditions, and to identify periods with active nucleation. The additional loss term S_{losses} (e.g., dilution due to boundary layer growth, wall losses) was negligible under our field conditions (Dal Maso et al., 2005). For regional NPF events, transport losses can also be ignored. FR is a direct measure of NPF intensity and is later compared across different meteorological and chemical conditions.

Condensable vapor concentration (C) and source rate (Q). Assuming that particle growth is dominated by condensation of a low-volatility vapor (typically sulfuric acid), the vapor concentration can be estimated from the observed growth rate (Dal Maso et al., 2005; Kulmala et al., 2012):

$$C = A \times \frac{dDp}{dt} \quad (5)$$

where D_p is the particle diameter, and A is a constant, which has the value 1.37×10^{-7} $h\cdot cm^{-3}\cdot nm^{-1}$ for a vapor with molecular properties of sulfuric acid(Dal Maso et al., 2005). This provides an upper-limit estimate of the condensable vapor concentration, as it assumes growth is solely due to condensation of the vapor and neglects contributions from coagulation.

The CS (Eq. 2) quantifies the rate at which this vapor is removed by pre-existing particles. Under steady-state conditions (dC/dt=0), the vapor source rate Q can be derived as (Dal Maso et al., 2005):

$$Q = CS \times C \quad (6)$$

This source rate represents the net production of condensable vapor needed to maintain the observed growth and is later compared with precursor gas concentrations (e.g., SO_2) to infer the chemical pathways driving NPF.

Hygroscopicity parameter (κ_{inorg}) for inorganic species. Due to the lack of organic composition measurements, we estimated the hygroscopicity of the inorganic fraction only. The measured water-soluble ions (SO_4^{2-}, NO_3^-, NH_4^+, Cl^-) were converted to mass concentrations of inorganic salts using the ion-pairing scheme described in Gysel et al. (2007) and Kuang et al. (2020). The following salts and their κ values (Kuang et al., 2020, Table S2) were considered: $(NH_4)_2SO_4$ (κ = 0.48), NH_4NO_3 (κ = 0.58), NH_4HSO_4 (κ = 0.56), and NH_4Cl (κ = 0.93). The volume fraction of each salt was calculated using its density (also from Kuang et al., 2020). The overall inorganic hygroscopicity parameter κinorg was then obtained by volume-weighted mixing (Petters and Kreidenweis, 2007):

$$\kappa_{inorg} = \sum_i \varepsilon_i \kappa_i \quad (7)$$

where κ_i and ε_i represent the hygroscopicity parameter and volume fraction of component i in the mixture, respectively, and i denotes the number of components. This κinorg represents the hygroscopicity of the inorganic aerosol components and is used as an upper limit estimate for the total particle hygroscopicity, as organic matter (typically less hygroscopic) was not included.

The concentrations of secondary organic carbon (SOC) and primary organic carbon (POC) were estimated following (Wu and Yu, 2016):

$$POC = (OC/EC)_{min} \times EC \quad (8)$$

$$SOC = OC_{total} - (OC/EC)_{pri} \times EC \quad (9)$$

where OC_{total} is the measured OC, $(OC/EC)_{min}$ is the minimum (OC/EC) ratio during the observation period, POC is primary organic carbon, and SOC is secondary organic carbon.

The enhancement effect on cloud condensation nuclei number concentration (E_N_{CCN}) was defined as the ratio of CCN number concentration after the NPF event to that before the event (Ren et al., 2021):

$$E\_N_{CCN} = N_{CCN,\,after} / N_{CCN,\,prior} \quad (10)$$

where $N_{CCN,\,after}$, is the average CCN number concentration during the NPF event (from its start to end), and $N_{CCN,\,prior}$, is the average CCN concentration during the 2 h before the event. This factor directly links NPF to potential cloud formation: a value >1 indicates that NPF increases CCN availability.

XGBoost-SHAP framework. To quantitatively evaluate the nonlinear effects of meteorological factors (T, RH) and precursor gases (NH_3, SO_2) on the particle formation rate (FR), we applied an interpretable machine learning framework combining XGBoost (Extreme Gradient Boosting) with SHAP (SHapley Additive exPlanations). A detailed description of the feature selection, model training, validation, and SHAP interpretation is provided in the supplementary material (Text S1). The main quantitative thresholds and interaction strengths derived from this analysis are discussed in Section 3.4.

2.4 Identification of NPF events

NPF events were identified based on criteria from Kulmala et al. (2012): (1) significant increase in nucleation-mode number concentration (N_{nuc}) (diameter 10–25 nm); (2) formation of a new mode lasting several hours; (3) growth of the newly formed mode over several hours. Additional criteria for NPF

identification included: low pre-existing particle number concentration, a clear "banana-shaped" evolution in particle number concentration over time and size, and exclusion of interference from pre-existing particles (especially in urban environments) (Heintzenberg et al., 2007).

In this study, a day was defined as an effective NPF day if the nucleation-mode (10–25 nm) particle number concentration increased continuously for at least 2 h from its initial value to its maximum and showed clear growth to larger sizes (e.g., 12–50 nm) over several hours (Fig. 1). Other days were defined as non-NPF days (Leng et al., 2014). During the one-year observation, a total of 46 NPF events and 319 non-NPF days were identified.

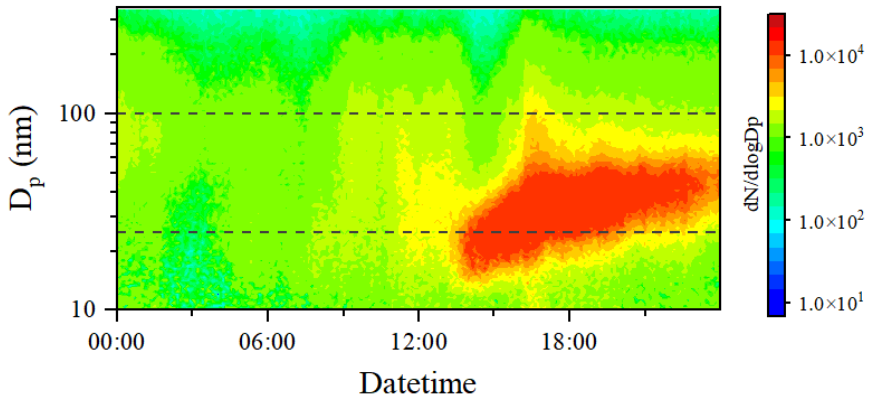

Fig. 1 An example NPF event observed on 21 April 2022.

3 Results and Discussion

3.1 Overall characteristics of NPF occurrence

NPF events in Fuzhou exhibited a distinct seasonal preference. As shown in Fig. 2a, spring was the season with the highest NPF frequency (27.17 %), while summer had the lowest (4.35 %). Fall (9.89 %) and winter (8.89 %) showed intermediate to low frequencies. NPF events mainly occurred between 9:00 and 12:00.

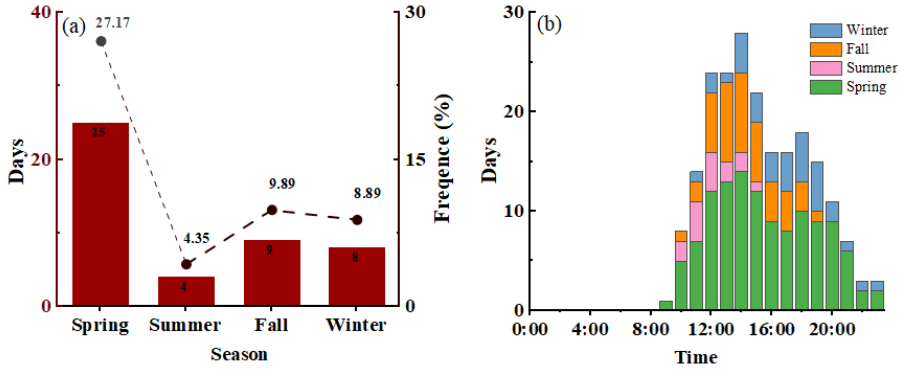

Fig. 2 The occurrence frequency and diurnal distribution of NPF events.

NPF events led to significant increases in nucleation-mode (N_{nuc}) and Aitken-mode (N_{ait}) particle number concentrations (Fig. S1). Spring showed the highest increase in N_{nuc} (196.7%), while fall showed the highest increase in N_{ait} (70.5%), indicating differences in new particle formation and subsequent growth across seasons.

NPF days typically corresponded to a lower background of $PM_{2.5}$ and PM_{10} (Fig.S3), indicating that NPF occurred in relatively clean atmospheres with a weak condensation sink. It should be noted that the absolute $PM_{2.5}$ and PM_{10} in winter and spring were still relatively high compared to other seasons (Fig.S3), implying that even on NPF days. In spring, summer, and winter, POC on NPF days were lower than on non-NPF days, corroborating this point. Meanwhile, in spring, summer, and fall, SOC was higher on NPF days, suggesting that secondary organic vapors may actively participate in particle formation and growth.

Although spring and winter had heavy background pollution, Fig.S4 shows that the gaseous precursor SO_2 concentration on NPF days was significantly higher than on non-NPF days (winter: 0.88 vs. 0.76 $\mu g \cdot m^{-3}$; spring: 0.64 vs. 0.53 $\mu g \cdot m^{-3}$). This indicates that in polluted seasons, high gaseous precursors can overcome the inhibitory effect of a high CS and thus trigger nucleation. In contrast, NPF days in summer and Fall exhibited a distinctly clean background, with NH_3 and HNO_2 significantly lower than on non-NPF days (Fig.S4). In summer, fall, and winter, the concentrations of sulfate (SO_4^{2-}), nitrate (NO_3^-), and ammonium (NH_4^+) on NPF days were significantly lower than on non-NPF days (Fig.S5). This suggests that in these seasons, the lower pre-existing particles and the reduced CS lessen the consumption of gaseous precursors, thereby favouring new particle formation and subsequent growth. However, spring presents a special case in that the SNA (sulfate, nitrate, and ammonium) concentrations on NPF days

were comparable to those on non-NPF days (SO_4^{2-}: 4.35 vs. 4.27 μg·m^{-3}). This indicates that spring NPF events are driven by high precursor concentrations. Even when the background particle level is high, the abundant supply of gaseous precursors (Fig. S4) can still overcome the inhibition and trigger NPF events. According to the hygroscopicity parameter (κ_{inorg}) shown in Fig. S6, the κ_{inorg} values on NPF days were generally lower than on non-NPF days in all seasons except summer, which is generally attributed to an increased proportion of weakly hygroscopic components in newly formed particles. However, the κ_{inorg} on NPF days was significantly higher than on non-NPF days in summer. Combined with the higher Cl^- concentration on summer NPF days in Fig. S5 (0.59 vs. 0.28 μg·m^{-3}). Despite reduced hygroscopicity, NPF events effectively increased N_{CCN}. At SS above 0.4 %, N_{CCN} on NPF days was higher than on non-NPF days in all seasons except spring, with the most significant increases observed in winter and fall (Fig.S7).

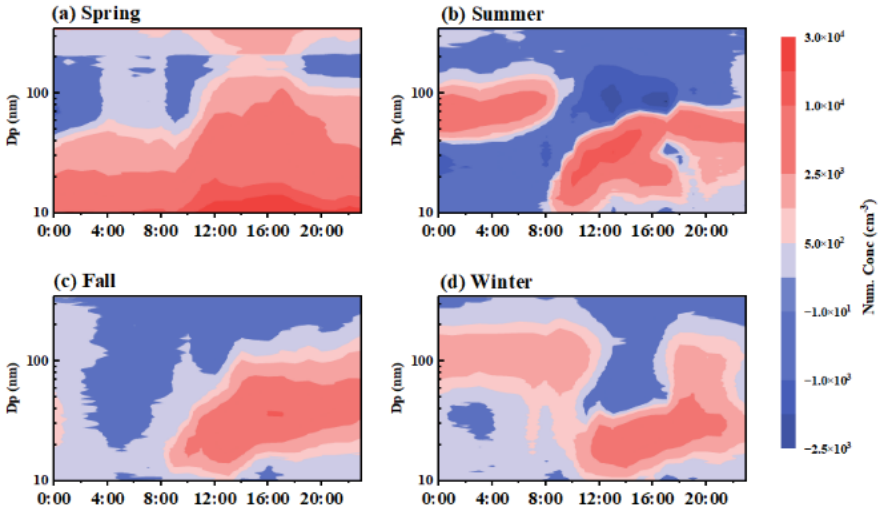

Fig. 3 The differences in particle number size distributions between NPF days and non-NPF days for each season.

Fig. 3a shows that in spring, particle number concentrations in the 10–20 nm range are generally elevated. NPF typically occurs from 9:00 to 20:00, with the peak concentration of 10–15 nm particles reaching 29,498 cm^{-3}. Concurrently, the concentration of particles >20 nm increases significantly, with some growing beyond 100 nm. The aerosol size distributions on NPF days in summer, fall, and winter all exhibit an NPF process pattern similar to that shown in Fig. 1, typically occurring in 09:00–20:00. During summer NPF events, the maximum particle number concentration reaches approximately 11,410 cm^{-3}, with particles growing up to around 50 nm. In fall and winter, peak particle number concentrations are

lower than in summer (10110 and 5276 cm^{-3}), indicating weaker NPF intensity, and the maximum particle growth can extend up to 100 nm in these seasons.

3.2 Evolution characteristics and key parameters of NPF events

Spring NPF events had the highest formation rate (FR=7.13 $cm^{-3}\cdot s^{-1}$) and the highest condensation sink (CS=4.1×10^{-2} s^{-1}) among all seasons (Table 1). Before NPF events (-4 to 0 h), N_{nuc} increased from 5425 to 7701 cm^{-3}, peaking at 1 h (8840 cm^{-3}), then gradually declining. This trend was consistent with changes in the FR (Fig. 4a). FR rose sharply to 6.31 $cm^{-3}\cdot s^{-1}$ at the onset of NPF (0 h) and peaked at 7.21 $cm^{-3}\cdot s^{-1}$ at 1 h, demonstrating strong new particle formation capability. However, intense competition under a high CS background significantly suppressed subsequent growth. The growth rate (GR) exhibited large fluctuations, reverting to a negative value at 3 h after an initial peak. N_{ait} increased by only 32 % from 0 h to its peak at 2 h, much lower than in other seasons. Spring NPF events were characterized by strong formation but suppressed growth under high CS.

Table 1. Seasonal variations in key parameters of NPF events: particle growth rate (GR), formation rate (FR), coagulation sink (CoagS), condensable vapor concentration (C) and its production rate (Q), condensation sink (CS), and hygroscopicity parameter (κ).

Average	FR ($m^{-3}\cdot s^{-1}$)	GR ($nm\cdot h^{-1}$)	CS ($\times10^{-2}\cdot s^{-1}$)	CoagS ($\times10^{-4}\ s^{-1}$)	C ($\times10^{7}\ cm^{-3}$)	K_{inorg}
Total	3.94	5.20	3.1	3.9	16.7	0.56
Spring	7.13	3.69	4.1	5.2	20.1	0.54
Summer	0.40	4.20	1.8	2.0	10.9	0.59
Fall	0.28	2.35	2.0	1.8	9.5	0.55
Winter	0.23	1.87	2.1	1.9	4.7	0.58

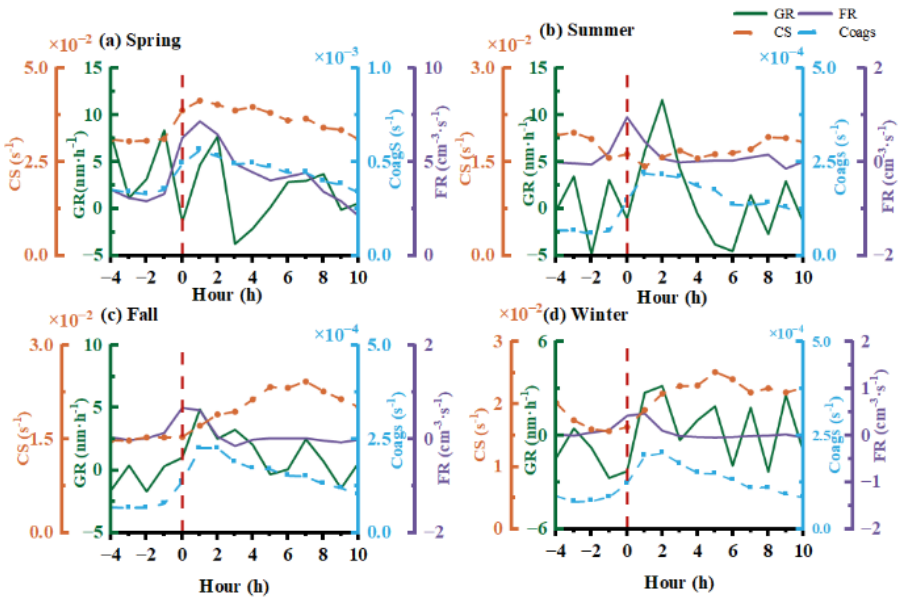

Fig. 4 Key NPF parameters: growth rate (GR), formation rate (FR), condensation sink (CS), and coagulation sink (CoagS) for each season. The NPF events in each season have been normalized. The x-axis represents time relative to the NPF event start, where t=0 h is the onset time (defined as the time when the nucleation-mode particle number concentration begins a sustained increase). Negative times indicate hours before the start, and positive times indicate hours after the start. The time axis ranges from –4 h to 10 h, showing the evolution from 4 hours before to 10 hours after the event.

Despite the low average FR (0.40 $cm^{-3}·s^{-1}$, Table 1), summer exhibited the highest average GR (4.20 $nm·h^{-1}$), and the lowest average CS ($1.8×10^{-2}$ s^{-1}). In summer NPF events (Fig. 4b), N_{nuc} peaked at 1 h (3459 cm^{-3}). FR relatively high from 0–2 h (0.97–0.44 $cm^{-3}·s^{-1}$). The most prominent feature of summer was the high growth efficiency (GR) under the lowest CS, with a maximum peak of 11.68 $nm·h^{-1}$ at 2 h. After NPF onset in summer, N_{ait} peaked at 3 h (6461.6 cm^{-3}), with the highest increase of 202.91 %. This indicates that the growth process of new particles in summer NPF events was far stronger than particle formation.

Winter had the lowest average FR (0.23 $cm^{-3}·s^{-1}$) and GR (1.87 $nm·h^{-1}$, Table 1). Winter NPF events were characterized by a low FR and delayed growth under a low condensation sink (CS), as shown in Table 1. In Fig.4d, the FR peak observed at 0 h (0.43 $cm^{-3}·s^{-1}$) was the lowest among all seasons, indicating weak nucleation. In contrast, the growth rate (GR) displayed a distinct multi-peak pattern, with an initial peak at 2 h (3.20 $nm·h^{-1}$) and subsequent peaks occurring between 5 and 9 h, suggesting that different mechanisms may have driven particle growth at different stages. Correspondingly, N_{ait} reached a maximum at 3 h (4794.2 cm^{-3}), which was the lowest seasonal peak (Fig.S8). Nevertheless, N_{ait}

remained at relatively high levels (4500–4800 cm^{-3}) over an extended period from 2 to 6 h, reflecting sustained particle growth throughout the event.

Fall presented transitional characteristics, with average FR (0.28 $cm^{-3}·s^{-1}$) and GR (2.35 $nm·h^{-1}$) higher than winter but lower than spring and summer (Table 1). Fall NPF process parameters showed transitional characteristics between summer and winter, generally similar to winter (Fig. 4c). Its FR peak (0.68 $cm^{-3}·s^{-1}$) and GR peak (4.90 $nm·h^{-1}$) were higher than winter but much lower than spring and summer. The increase in N_{ait} after NPF onset was 165 %, significantly stronger than in winter (Fig.S8). The N_{ait} peak (6240.9 cm^{-3}) occurred latest (4 h) and remained above 5600 cm^{-3} from 5–7 h, higher than winter.

In summary, spring shows the highest FR (7.13 $cm_{-3}·s^{-1}$) but the lowest GR (3.69 $nm·h^{-1}$) due to a large CS, indicating strong nucleation yet suppressed growth. Summer achieves the highest GR (peak 11.68 $nm·h^{-1}$) and the cleanest background (lowest CS), where growth dominates over formation. Fall and winter exhibit low FR and GR with delayed growth, reflecting weaker NPF intensity.

3.3 Influence of chemical composition on NPF events

Spring NPF days were characterized by the highest CS ($4.1×10^{-2}$ s^{-1}) and were predominantly influenced by secondary pollution. Spring NPF events were mainly driven by the continuous transport from the southeast coastal pathway (CL2, 51.33%, Fig. S8a), which supplied high levels of NH_3 (6.76±2.09 $μg·m^{-3}$) and HNO_2 (2.81±2.16 $μg·m^{-3}$) (Table S4). Consistently, during the NPF events, the frequency of SE/S winds continuously increased and became dominant in the later stage (maximum 38.1%), reflecting the influence of this coastal air mass at the local scale. Before NPF events, gaseous SO_2 and NH_3 increased from 0.47 and 5.01 $μg·m^{-3}$ to 0.89 and 5.95 $μg·m^{-3}$, respectively (Fig. 5a). Two hours after NPF onset, their concentrations began to decline continuously, indicating substantial consumption. Mass concentrations of secondary inorganic salts (SO_4^{2-} and NO_3^-) fluctuated between 4.5–4.8 $μg·m^{-3}$ and 4–6 $μg·m^{-3}$, respectively. Although NO_3^- showed minor fluctuations, it remained at relatively high levels (Fig. 6a). NPF events occurred when the temperature was between 18.9–23.2°C (Fig. S11a), favoring accelerated photochemical reactions and gas-particle conversion of semi-volatile gases (Chen et al., 2023). Wind speeds were generally low (<1.9 $m·s^{-1}$), and the atmospheric stratification was stable. After NPF onset, O_3 increased significantly (from 81.1 to 98.8 $μg·m^{-3}$; Fig. S13a), indicating enhanced atmospheric oxidizability. Precursor gases (SO_2 and NO_2) were oxidized via photochemistry to form

NO_3^- and SO_4^{2-}, promoting the generation of secondary inorganic salts and secondary aerosols, including secondary organic aerosol (Fig. S12a). The high CS background, spring had high-frequency and high-FR NPF events, primarily attributed to higher precursor gas and strong photochemistry.

However, high CS competed for condensable vapors and scavenged newly formed particles, suppressing the growth stage of new particles. Additionally, during the NPF event (1–4 h), particle hygroscopicity decreased from 0.56 at -4 h to 0.53 (fig.S10).

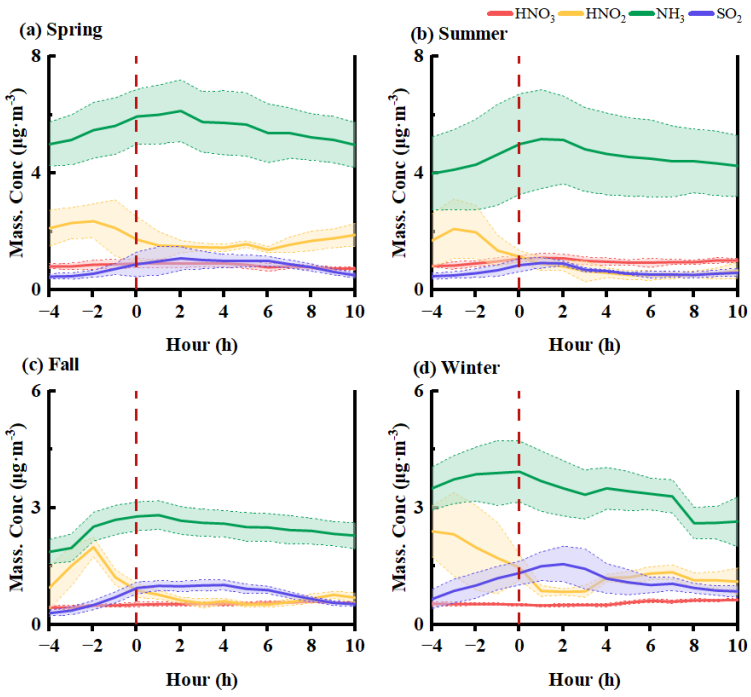

Fig. 5 The evolution of relevant trace gases (SO_2, NH_3, NO_2) for (a) spring, (b) summer, (c) fall, and (d) winter. The x-axis follows the same normalized time scale as defined in Fig. 4 (t = 0 h represents NPF event start). Shaded bands indicate ±1σ standard deviation

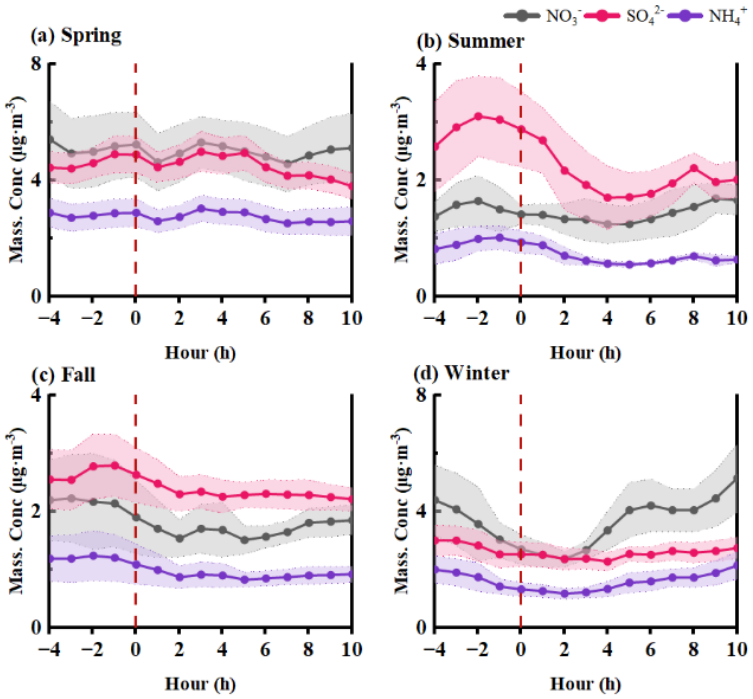

Fig. 6 The evolution of major secondary inorganic ions (SO_4^{2-}, NO_3^-, NH_4^+) for each season. The x-axis follows the same normalized time scale as defined in Fig. 4 (t=0 h represents NPF event start). Shaded bands indicate ±1σ standard deviation.

CS in summer, fall, and winter were relatively low (around 2.0×10^{-2} s^{-1}), indicating fewer surfaces available for condensation in the atmosphere.

Summer NPF events occurred under a high-temperature environment (>32°C) (Fig. S9b), which inhibits nucleation (Yu et al., 2017). Two hours after NPF onset (2 h), the frequency of northeasterly (NE) winds surged from 0% (at -4 h) to 50%, corresponding to marine air mass cluster CL2 (60%), which had a low average CS of $1.08 \pm 0.31\times10^{-2}$ s^{-1}(Table S3). The arrival of this air mass diluted local pollutants, causing PM_{10} to drop from 14.25 μg·m^{-3} at 0 h to 8.75 μg·m^{-3} at 2 h; meanwhile, it supplied abundant gaseous precursors or enhanced local photochemical activity, leading to continuous increases in SO_2 and NH_3 from 0.48 and 4.00 μg·m^{-3} to peak values of 0.94 and 5.18 μg·m^{-3}, respectively, at 2 h (Fig. 5b). Therefore, despite favorable conditions of low CS and ample sunlight, summer NPF frequency and formation rate were low. As ozone continued to rise (0–6 h), secondary ions (NO_3^-, SO_4^{2-}) and SOC increased (Fig. 6b and Fig. S12b). These efficiently condensed onto particle surfaces under a low CS background, achieving extremely high growth efficiency (GR peak of 11.59 nm·h^{-1}). κ_{inorg} in the range of 0.61–0.75 was higher than in other seasons, surging to 0.75 at 3 h after NPF onset. This increase was primarily driven by

prevailing easterly and southerly winds, corresponding to air mass cluster CL3, which had a high κ_{inorg} (0.71). This indicates that inorganic salts of marine origin facilitated the sustained growth of particles. Before Fall NPF events, SO_2 and NH_3 increased from 0.36 and 1.99 $\mu g \cdot m^{-3}$ to 2.83 and 2.83 $\mu g \cdot m^{-3}$, respectively (Fig. 5c). This stage was dominated by northwesterly winds (NW: 62%) and strongly influenced by continental air masses from CL2 and CL3, which contributed to the initial accumulation of precursor gases (SO_2 and NH_3). The lower temperature (around 22 °C) and high humidity (RH >71 %) environment (Fig. S11c) favored the combination of sulfuric acid molecules, promoting nucleation (Lehtipalo et al., 2018; Tröstl et al., 2016; Yue and Hamill, 1979). After NPF onset, although atmospheric oxidizability increased continuously (O_3 from 36 to 94 $\mu g \cdot m^{-3}$), it was short-lived. Within 1–3 h after NPF onset, the local wind direction shifted notably to southerly (S: 44.4%, Fig.S9c), corresponding on a larger scale to the marine/coastal air mass trajectory CL1 (22.22%, Fig.S8c). CL1 served as the most important transport pathway for NH_3 in the fall, with an average concentration as high as 3.13 $\mu g \cdot m^{-3}$ (Table S4), substantially higher than that of continental pathways. After 4 h, as O_3 gradually decreased and primary emissions increased, pollutant accumulation occurred, and BC and POC rebounded (Fig. S12c). The contribution of primary emissions (e.g., BC, POC) to aerosols was significantly enhanced, and overall κ_{inorg} (0.55) was low.

Winter NPF events were also preceded by an accumulation of gaseous precursors (Fig. 5d). However, elevated emissions from sources such as heating led to high BC and POC during the initial NPF stage (1.86 and 1.02 $\mu g \cdot m^{-3}$ at -4 h, Fig. S12d). These abundant primary particles strongly suppressed new particle formation via intense coagulation scavenging, resulting in persistently low formation rates (FR $\leqslant$0.47 $cm^{-3} \cdot s^{-1}$). Photochemical activity was limited under low winter temperatures (Fig. S11d). As temperatures continued to drop later in the event (after 6 h), condensation-driven conversion of gaseous precursors to particles increased (Jokinen et al., 2018). During the 6–10 h period, the high concentrations of precursors reached supersaturation under the low-temperature conditions, promoting the rapid formation of particulate ammonium nitrate (nitrate concentration increased from 4.21 to 5.14 $\mu g \cdot m^{-3}$, Fig. 6d). In winter, the air masses were mainly dominated by the northwesterly continental air mass originating from Siberia (CL1, Fig.S8d). Particles within this air mass exhibited relatively high κ_{inorg} (0.59, Table S3), and the introduction of these hygroscopic components effectively offset the dilution of

overall hygroscopicity caused by BC and POC. During the 8–10 h period, northwesterly winds persisted, and their frequency gradually increased, which also explains the gradual increase in κ_{inorg} values (from 0.57 to 0.61, Fig.S10).

In summary, in spring, high NH_3 and photochemistry drive strong nucleation, but high CS and secondary inorganic salts suppress growth. Summer marine air masses provide low CS and high hygroscopicity (κ_{inorg} > 0.6), favoring efficient growth, while fall and winter continental emissions (BC, POC) lower κ_{inorg} (≤0.55) and limit NPF intensity.

3.4 Attribution analysis of particle formation and growth

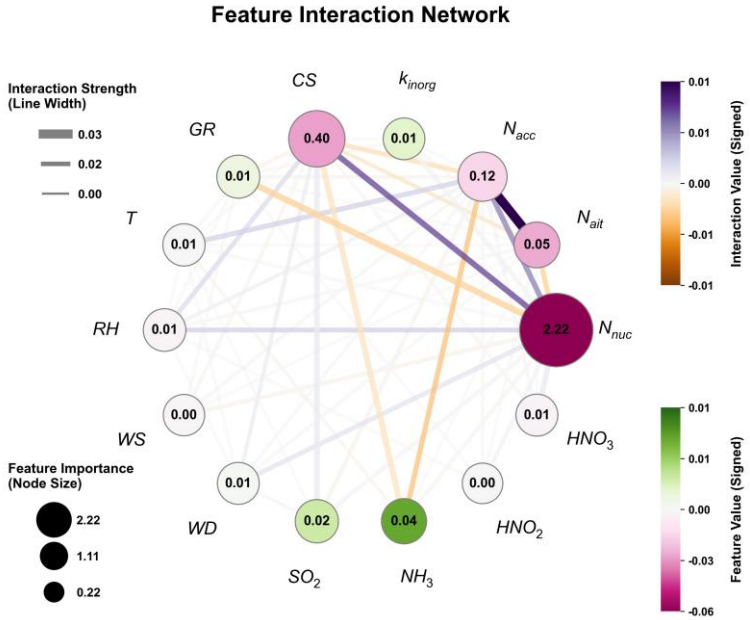

Fig. 7 Non-linear response relationships and interaction analysis between core environmental factors and FR. Node size and inner numbers denote feature importance (mean |SHAP|). Node color indicates contribution direction (green: positive; pink: negative). Edge width reflects interaction strength; edge color indicates interaction direction (purple: synergistic; orange: antagonistic).

According to SHAP analysis (Fig.S14), the main contributors to FR in Fuzhou are nucleation mode (76.2%), CS (13.8%), NH_3 (1.3%), and SO_2 (0.6%). Physical processes explain ~90% of the variance. A prominent feature is the sharp NH_3 threshold at 4 $\mu g \cdot m^{-3}$: below this, SHAP ≈ -0.025; above, it turns positive and rises by 0.2 at 10 $\mu g \cdot m^{-3}$. CS shows a clear inhibition onset at 0.03 s^{-1}, with SHAP dropping from 0 to -0.5 as CS increases to 0.08 s^{-1}. Temperature has a positive SHAP only within 20–25°C (peak ~0.01), decreasing by 40% at 35°C. As shown in Fig. 7, the strongest interaction is between nucleation

mode and CS (0.40), far exceeding other pairs (NH_3-nucleation mode: 0.04), highlighting that the net FR is governed by the competition between particle formation and scavenging.

For the Aitken mode, the driving forces shift notably. CS remains the top contributor, followed by accumulation mode (13.8%) and nucleation mode (7.1%). As shown in Fig.S15, a key distinction from FR is the temperature response. Instead of a bell shape, SHAP increases linearly from 0 to 0.1 over 20–35°C, indicating that high temperatures accelerate particle growth, enabling a rapid transition from nucleation to the Aitken mode. The NH_3 threshold at 4 $\mu g \cdot m^{-3}$ persists, showing its continued role in particle growth. RH exerts a linear negative effect, turning SHAP negative above 60%, suggesting hygroscopic growth or coagulation loss. In Fig.S16, the CS-nucleation mode interaction strength is 0.12, lower than in FR but still dominant, implying that strong nucleation can offset high CS losses.

In summary, the SHAP attribution reveals two distinct regimes. FR is dominated by CS, accompanied by a sharp chemical trigger ($NH_3 > 4$ $\mu g \cdot m^{-3}$) and a narrow temperature window (20–25°C). The Aitken mode, while still influenced by CS, is primarily driven by temperature-accelerated growth (linearly increasing above 20°C). Ammonia acts as a persistent enhancer in both stages, whereas high RH (>60%) consistently suppresses Aitken mode concentrations.

3.5 Particle growth controls CCN formation from NPF events

In summer, although NPF frequency was the lowest, it had a significant enhancing effect on N_{CCN}. E_N_{CCN} at 0.4 % SS was as high as 1.64 (Fig. 8a). In the initial stage of NPF events (0–2 hours), N_{CCN} showed a sharp decline. At 0.4 % SS, it decreased from about 2078 cm^{-3} to 1187 cm^{-3} (Fig. S17b). However, after 2 h, N_{CCN} recovered noticeably and later returned to or even exceeded initial levels. The CCN size distribution (Fig. 8c) showed that during the event, smaller CCN (1–3 μm) decreased, while CCN of 5.5–6.5 μm increased. For instance, CCN at 6 μm increased from 2607.7 to 3147.8 cm^{-3}. Summer NPF promoted CCN growth to larger sizes. However, the daily average N_{CCN} on summer NPF days was lower than on non-NPF days, possibly due to the extremely low NPF frequency (4.35 %) and the sharp decline in CCN at the beginning of events, affecting the daily average.

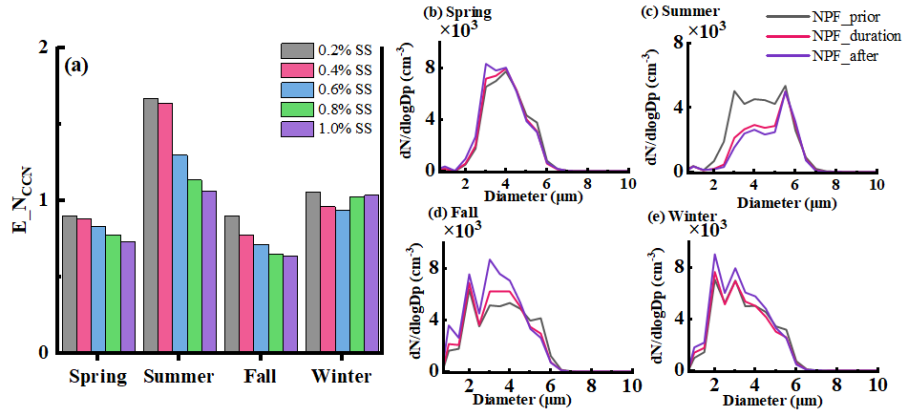

Fig.8 The contribution of NPF events to cloud condensation nuclei (CCN) across seasons: (a) CCN enhancement (E_N_{CCN}), and (b-e) particle number size distributions at 2 hours before, during, and 5 hours after the NPF event for seasons.

Spring NPF events' impact on N_{CCN} showed significant suppression. Throughout the event, N_{CCN} at various supersaturation levels showed only weak and slow increases. N_{CCN} (0.4 % SS, the same as below) increased from a pre-event average (-4 to -1 h) of about 2636 cm^{-3} to 3192 cm^{-3} at 4 h, then decreased slowly from 4 to 6 h, with a larger decline at higher supersaturations (Fig. S17a). E_N_{CCN} at 0.4 % SS was only 0.88. This phenomenon corresponds to the "high formation, suppressed growth" characteristic of spring NPF. Despite the explosive generation of nucleation-mode particles, severe competition under high CS severely hindered subsequent growth of new particles, preventing them from effectively growing to CCN activation sizes, resulting in a weak or even negative contribution to CCN.

In fall events, from 2 h onward, N_{CCN} began to increase, rising from 3471 cm^{-3} to a maximum of 4752 cm^{-3}, forming a high-value plateau lasting from 3 to 8 h (Fig. S17d). After the NPF event, N_{CCN} increased significantly across the 1-5 μm size range (Fig. 8d). Fall NPF events most effectively and broadly increased the number of particles available for cloud droplet activation in the atmosphere. Although E_N_{CCN} was lower due to the modest initial stage, the post-event enhancement effect was significant. This evolution process is consistent with the sustained particle growth process in fall NPF, allowing new particles to grow steadily to CCN activation sizes.

In winter NPF events, N_{CCN} was low in the early stage (0–4 h), with insignificant growth. However, from 5 h onward, N_{CCN} growth became significant, increasing from 4483 cm^{-3} to 6173 cm^{-3} and remaining stable at high levels (Fig. S17d). During the event, changes in the CCN size distribution were not obvious.

However, after the NPF event, CCN in the 2–5 μm size range showed the most significant growth (e.g., at 2 μm, from 7073.0 to 9045.1 cm^{-3}; Fig. 8e).

4 Conclusions

This year-long observational study in coastal Fuzhou revealed distinct seasonal patterns in new particle formation (NPF) and its impact on cloud condensation nuclei (CCN). We identified 46 NPF events, which predominantly occurred between 09:00 and 12:00. Key quantitative results include: the highest seasonal formation rate (FR) in spring (5.56 cm^{-3} s^{-1}), the highest growth rate (GR) in summer (peak at 11.68 nm h^{-1}), and the strongest CCN enhancement in summer (E_N_{CCN} = 1.64 at 0.4 % SS). In fall and winter, CCN increases (13–65 %) lag NPF events by 3–5 h.

A total of 46 NPF events occurred during the observation period, with a frequency of 12.7 %. NPF event start times were mainly concentrated between 08:00 and 13:00 (accounting for 85 % of all events), with an average duration of 4 h. The annual averages for formation rate (FR), growth rate (GR), condensation sink (CS), coagulation sink (CoagS), and condensable vapor concentration (C) were 3.94 ± 8.26 $cm^{-3}\cdot s^{-1}$, 5.20 ± 1.78 $nm\cdot h^{-1}$, 4.2×10^{-2} s^{-1}, 5.6×10^{-4} s^{-1}, and 16.7×10^{7} cm^{-3}, respectively.

The seasonal contrast is mechanistically driven by the interplay between precursor availability, CS, and aerosol chemistry. Spring conditions favor high FR due to strong photochemistry and abundant precursors, but high CS suppresses subsequent growth. In summer, the occurrence of NPF events is often accompanied by a transition in sea-land breeze circulation. The northerly land breeze shifts to northeasterly/easterly sea breezes, effectively transporting clean marine air masses to the observation site. This reduces the CS to its seasonal minimum ($1.08\pm0.31\times10^{-2}$ s^{-1}), favoring efficient particle growth and thereby sustaining the highest growth rate (GR) observed across all seasons. The chemical composition shifts from being dominated by sulfate and sea salt with high hygroscopicity in summer (κ_{inorg} > 0.6) to low hygroscopicity in fall (κ_{inorg}=0.55), directly modulating particle hygroscopicity and cloud condensation nuclei (CCN) activation potential.

Using XGBoost-SHAP, FR is dominated by nucleation mode (76.2 %) and CS (13.8 %). NH_3 > 4 $\mu g\cdot m^{-3}$ enhances FR, CS > 0.03 s^{-1} inhibits FR (SHAP drops to –0.5 at 0.08 s^{-1}), and Temperature benefits FR only within 20–25 °C. For Aitken mode, temperature linearly promotes growth above 20°C, while

RH > 60 % suppresses it. The strong nucleation-CS interaction (0.40) highlights the competition between formation and scavenging.

This work demonstrates that the climatic impact of NPF in coastal urban areas is not simply a function of its occurrence frequency or formation strength. Instead, it is seasonally modulated by a competition between formation and growth-sink processes, and by the resulting aerosol chemical composition. The decoupling of high FR from effective CCN production (as in spring) implies that climate models using NPF frequency as a proxy for aerosol indirect effects may overestimate the impact in high-CS coastal regions. Conversely, the efficient growth and CCN enhancement in summer suggest that even infrequent NPF events can substantially influence cloud properties in such environments. These insights are crucial for developing more accurate parameterizations of aerosol-cloud-climate interactions in rapidly developing coastal zones.

Data availability

Data will be made available on request.

Author contributions

Conceptualization was completed by ZW and HW. Formal analysis and software modification were carried out by ZW and HW. The initial draft was written by ZW, incorporating tables provided by HW. The first draft was revised by ZW, HW, and YB, with input from HW, YB, FZ, WL, JH, LS, and ZX; subsequent versions of the manuscript were reviewed and edited by all authors. Data curation and collection were conducted by all authors. Funding acquisition was secured by HW.

Competing interests

The authors declare that they have no conflict of interest.

Disclaimer

Copernicus Publications remains neutral with regard to jurisdictional claims made in the text, published maps, institutional affiliations, or any other geographical representation in this paper. While Copernicus

Publications makes every effort to include appropriate place names, the final responsibility lies with the authors. Views expressed in the text are those of the authors and do not necessarily reflect the views of the publisher.

Acknowledgements

The authors are grateful for the assistance with sample collection. We would like to thank the China National Environmental Monitoring Centre's real-time urban air quality release platform (http://106.37.208.233:20035/)

Financial support

This study was supported by the National Key Research and Development Program of China (Grant No., 2022YFC3701204), the National Natural Science Foundation of China (42505181 and U22A20578), Natural Science Foundation of Fujian Province, China (2024J01168 and 2023R1014003), the Natural Science Foundation of Jiangsu Province (BK20231300), and the Open Fund of Fujian Key Laboratory of Severe Weather and Key Laboratory of Straits Severe Weather (2024KFKT05).

References

Battelle: Environmental Technology Verification Report: Applikon MARGA Semi-Continuous Ambient Air Monitoring System, U.S. Environmental Protection Agency, available at: https://nepis.epa.gov/Exe/ZyPURL.cgi?Dockey=P100FZOD.pdf (last access: 24 April 2026), 2009.

Cai, M., Tan, H., Chan, C. K., Qin, Y., Xu, H., Li, F., Schurman, M. I., Liu, L., and Zhao, J.: The size-resolved cloud condensation nuclei (CCN) activity and its prediction based on aerosol hygroscopicity and composition in the pearl delta river (PRD) region during wintertime 2014, Atmos. Chem. Phys., 18, 16419–16437, https://doi.org/10.5194/acp-18-16419-2018, 2018.

Chang, Y., Deng, C., Cao, F., Cao, C., Zou, Z., Liu, S., Lee, X., Li, J., Zhang, G., and Zhang, Y.: Assessment of carbonaceous aerosols in Shanghai, China–Part 1: long-term evolution, seasonal variations, and meteorological effects, Atmos. Chem. Phys., 17, 9945–9964, https://doi.org/10.5194/acp-17-9945-2017, 2017.

Chen, M., Titcombe, M., Jiang, J., Jen, C., Kuang, C., Fischer, M. L., Eisele, F. L., Siepmann, J. I., Hanson, D. R., Zhao, J., and McMurry, P. H.: Acid–base chemical reaction model for nucleation rates in the polluted atmospheric boundary layer, Proc. Natl. Acad. Sci., 109, 18713–18718, https://doi.org/10.1073/pnas.1210285109, 2012.

Dal Maso, M. D., Kulmala, M., Riipinen, I., Wagner, R., Hussein, T., Aalto, P., and Lehtinen, K.: Formation and growth of fresh atmospheric aerosols: eight years of aerosol size distribution data from SMEAR II, hyytiälä, Finland, Boreal Environ. Res., 10, 323–336, 2005.

Du, H., Kong, L., Cheng, T., Chen, J., Yang, X., Zhang, R., Han, Z., Yan, Z., and Ma, Y.: Insights into ammonium particle-to-gas conversion: non-sulfate ammonium coupling with nitrate and chloride, Aerosol Air Qual. Res., 10, 589–595, https://doi.org/10.4209/aaqr.2010.04.0034, 2010.

Dunne, E. M., Gordon, H., Kürten, A., Almeida, J., Duplissy, J., Williamson, C., Ortega, I. K., Pringle, K. J., Adamov, A., Baltensperger, U., Barmet, P., Benduhn, F., Bianchi, F., Breitenlechner, M., Clarke, A., Curtius, J., Dommen, J., Donahue, N. M., Ehrhart, S., Flagan, R. C., Franchin, A., Guida, R., Hakala, J., Hansel, A., Heinritzi, M., Jokinen, T., Kangasluoma, J., Kirkby, J., Kulmala, M., Kupc, A., Lawler, M. J., Lehtipalo, K., Makhmutov, V., Mann, G., Mathot, S., Merikanto, J., Miettinen, P., Nenes, A., Onnela, A., Rap, A., Reddington, C. L. S., Riccobono, F., Richards, N. A. D., Rissanen, M. P., Rondo, L., Sarnela, N., Schobesberger, S., Sengupta, K., Simon, M., Sipilä, M., Smith, J. N., Stozkhov, Y., Tomé, A., Tröstl, J., Wagner, P. E., Wimmer, D., Winkler, P. M., Worsnop, D. R., and Carslaw, K. S.: Global atmospheric particle formation from CERN CLOUD measurements, Science, 354, 1119–1124, https://doi.org/10.1126/science.aaf2649, 2016.

Chen, Y., Wang, X., Dai, W., Wang, Q., Guo, X., Liu, Y., Qi, W., Shen, M., Zhang, Y., Li, L., Cao, Y., Wang, Y., and Li, J.: Particle Number Size Distribution of Wintertime Alpine Aerosols and Their Activation as Cloud Condensation Nuclei in the Guanzhong Plain, Northwest China, J. Geophys. Res.: Atmos., 128, e2022JD037877, https://doi.org/10.1029/2022JD037877, 2023.

Fan, J., Rosenfeld, D., Zhang, Y., Giangrande, S. E., Li, Z., Machado, L. A. T., Martin, S. T., Yang, Y., Wang, J., Artaxo, P., Barbosa, H. M. J., Braga, R. C., Comstock, J. M., Feng, Z., Gao, W., Gomes, H. B., Mei, F., Pöhlker, C., Pöhlker, M. L., Pöschl, U., and de Souza, R. A. F.: Substantial convection and

precipitation enhancements by ultrafine aerosol particles, Science, 359, 411–418, https://doi.org/10.1126/science.aan8461, 2018.

Guo, S., Hu, M., Zamora, M. L., Peng, J., Shang, D., Zheng, J., Du, Z., Wu, Z., Shao, M., Zeng, L., Molina, M. J., and Zhang, R.: Elucidating severe urban haze formation in China, Proc. Natl. Acad. Sci., 111, 17373–17378, https://doi.org/10.1073/pnas.1419604111, 2014.

Heintzenberg, J., Wehner, B., and Birmili, W.: 'How to find bananas in the atmospheric aerosol': new approach for analyzing atmospheric nucleation and growth events, Tellus B, 59, 273–282, https://doi.org/10.1111/j.1600-0889.2007.00249.x, 2007.

Gysel, M., Crosier, J., Topping, D. O., Whitehead, J. D., Bower, K. N., Cubison, M. J., Williams, P. I., Flynn, M. J., McFiggans, G. B., and Coe, H.: Closure study between chemical composition and hygroscopic growth of aerosol particles during TORCH2, Atmos. Chem. Phys., 7, 6131–6144, https://doi.org/10.5194/acp-7-6131-2007, 2007.

Hamed, A., Korhonen, H., Sihto, S.-L., Joutsensaari, J., Järvinen, H., Petäjä, T., Arnold, F., Nieminen, T., Kulmala, M., Smith, J. N., Lehtinen, K. E. J., and Laaksonen, A.: The role of relative humidity in continental new particle formation, J. Geophys. Res.: Atmos., 116, D03206. https://doi.org/10.1029/2010JD014186, 2011.

Hirsikko, A., Nieminen, T., Gagné, S., Lehtipalo, K., Manninen, H. E., Ehn, M., Hõrrak, U., Kerminen, V.-M., Laakso, L., McMurry, P. H., Mirme, A., Mirme, S., Petäjä, T., Tammet, H., Vakkari, V., Vana, M., and Kulmala, M.: Atmospheric ions and nucleation: a review of observations, Atmos. Chem. Phys., 11, 767–798, https://doi.org/10.5194/acp-11-767-2011, 2011.

Hu, J., Shi, C., Ni, E., Liu, J., Zhai, S., Zhao, T., Jiang, B., Jiang, D., Wang, H., and Huang, Q.: Recirculated transport mechanism aggravates ozone pollution over the mountainous coastal region: Increased contribution from vertical mixing, Atmos. Environ., 332, 120617, https://doi.org/10.1016/j.atmosenv.2024.120617, 2024.

Jayaratne, R., Pushpawela, B., He, C., Li, H., Gao, J., Chai, F., and Morawska, L.: Observations of particles at their formation sizes in beijing, china, Atmos. Chem. Phys., 17, 8825–8835, https://doi.org/10.5194/acp-17-8825-2017, 2017.

Jokinen, T., Sipilä, M., Kontkanen, J., Vakkari, V., Tisler, P., Duplissy, E.-M., Junninen, H., Kangasluoma, J., Manninen, H. E., Petäjä, T., Kulmala, M., Worsnop, D. R., Kirkby, J., Virkkula, A., and Kerminen, V.-M.: Ion-induced sulfuric acid–ammonia nucleation drives particle formation in coastal antarctica, Sci. Adv., https://doi.org/10.1126/sciadv.aat9744, 2018.

Kawana, K., Miyazaki, Y., Omori, Y., Tanimoto, H., Kagami, S., Suzuki, K., Yamashita, Y., Nishioka, J., Deng, Y., Yai, H., and Mochida, M.: Number-Size Distribution and CCN Activity of Atmospheric Aerosols in the Western North Pacific During Spring Pre-Bloom Period: Influences of Terrestrial and Marine Sources, J. Geophys. Res.: Atmos., 127, e2022JD036690, https://doi.org/10.1029/2022JD036690, 2022.

Kirchstetter, T. W., Novakov, T., and Hobbs, P. V.: Evidence that the spectral dependence of light absorption by aerosols is affected by organic carbon, J. Geophys. Res.: Atmos., 109, 2004JD004999, https://doi.org/10.1029/2004JD004999, 2004.

Kirkby, J., Duplissy, J., Sengupta, K., Frege, C., Gordon, H., Williamson, C., Heinritzi, M., Simon, M., Yan, C., Almeida, J., Tröstl, J., Nieminen, T., Ortega, I. K., Wagner, R., Adamov, A., Amorim, A., Bernhammer, A.-K., Bianchi, F., Breitenlechner, M., Brilke, S., Chen, X., Craven, J., Dias, A., Ehrhart, S., Flagan, R. C., Franchin, A., Fuchs, C., Guida, R., Hakala, J., Hoyle, C. R., Jokinen, T., Junninen, H., Kangasluoma, J., Kim, J., Krapf, M., Kürten, A., Laaksonen, A., Lehtipalo, K., Makhmutov, V., Mathot, S., Molteni, U., Onnela, A., Peräkylä, O., Piel, F., Petäjä, T., Praplan, A. P., Pringle, K., Rap, A., Richards, N. A. D., Riipinen, I., Rissanen, M. P., Rondo, L., Sarnela, N., Schobesberger, S., Scott, C. E., Seinfeld, J. H., Sipilä, M., Steiner, G., Stozhkov, Y., Stratmann, F., Tomé, A., Virtanen, A., Vogel, A. L., Wagner, A. C., Wagner, P. E., Weingartner, E., Wimmer, D., Winkler, P. M., Ye, P., Zhang, X., Hansel, A., Dommen, J., Donahue, N. M., Worsnop, D. R., Baltensperger, U., Kulmala, M., Carslaw, K. S., and Curtius, J.: Ion-induced nucleation of pure biogenic particles, Nature, 533, 521–526, https://doi.org/10.1038/nature17953, 2016.

Kuang, Y., He, Y., Xu, W., Zhao, P., Cheng, Y., Zhao, G., Tao, J., Ma, N., Su, H., Zhang, Y., Sun, J., Cheng, P., Yang, W., Zhang, S., Wu, C., Sun, Y., and Zhao, C.: Distinct diurnal variation in organic aerosol hygroscopicity and its relationship with oxygenated organic aerosol, Atmos. Chem. Phys., 20, 865–880, https://doi.org/10.5194/acp-20-865-2020, 2020.

Kulmala, M., Vehkamäki, H., Petäjä, T., Dal Maso, M., Lauri, A., Kerminen, V.-M., Birmili, W., and McMurry, P. H.: Formation and growth rates of ultrafine atmospheric particles: a review of observations, J. Aerosol Sci., 35, 143–176, https://doi.org/10.1016/j.jaerosci.2003.10.003, 2004.

Kulmala, M., Petäjä, T., Nieminen, T., Sipilä, M., Manninen, H. E., Lehtipalo, K., Dal Maso, M., Aalto, P. P., Junninen, H., Paasonen, P., Riipinen, I., Lehtinen, K. E. J., Laaksonen, A., and Kerminen, V.-M.: Measurement of the nucleation of atmospheric aerosol particles, Nat. Protoc., 7, 1651–1667, https://doi.org/10.1038/nprot.2012.091, 2012.

Kulmala, M., Dada, L., Daellenbach, K. R., Yan, C., Stolzenburg, D., Kontkanen, J., Ezhova, E., Hakala, S., Tuovinen, S., Kokkonen, T. V., Kurppa, M., Cai, R., Zhou, Y., Yin, R., Baalbaki, R., Chan, T., Chu, B., Deng, C., Fu, Y., Ge, M., He, H., Heikkinen, L., Junninen, H., Liu, Y., Lu, Y., Nie, W., Rusanen, A., Vakkari, V., Wang, Y., Yang, G., Yao, L., Zheng, J., Kujansuu, J., Kangasluoma, J., Petäjä, T., Paasonen, P., Järvi, L., Worsnop, D., Ding, A., Liu, Y., Wang, L., Jiang, J., Bianchi, F., and Kerminen, V.-M.: Is reducing new particle formation a plausible solution to mitigate particulate air pollution in beijing and other chinese megacities?, Faraday Discuss., 226, 334–347, https://doi.org/10.1039/D0FD00078G, 2021.

Kuwata, M., Kondo, Y., Miyazaki, Y., Komazaki, Y., Kim, J. H., Yum, S. S., Tanimoto, H., and Matsueda, H.: Cloud condensation nuclei activity at Jeju Island, Korea in spring 2005, Atmos. Chem. Phys., 8, 2933–2948, https://doi.org/10.5194/acp-8-2933-2008, 2008.

Lehtipalo, K., Yan, C., Dada, L., Bianchi, F., Xiao, M., Wagner, R., Stolzenburg, D., Ahonen, L. R., Amorim, A., Baccarini, A., Bauer, P. S., Baumgartner, B., Bergen, A., Bernhammer, A.-K., Breitenlechner, M., Brilke, S., Buchholz, A., Mazon, S. B., Chen, D., Chen, X., Dias, A., Dommen, J., Draper, D. C., Duplissy, J., Ehn, M., Finkenzeller, H., Fischer, L., Frege, C., Fuchs, C., Garmash, O., Gordon, H., Hakala, J., He, X., Heikkinen, L., Heinritzi, M., Helm, J. C., Hofbauer, V., Hoyle, C. R., Jokinen, T., Kangasluoma, J., Kerminen, V.-M., Kim, C., Kirkby, J., Kontkanen, J., Kürten, A., Lawler, M. J., Mai, H., Mathot, S., MauldinIII, R. L., Molteni, U., Nichman, L., Nie, W., Nieminen, T., Ojdanic, A., Onnela, A., Passananti, M., Petäjä, T., Piel, F., Pospisilova, V., Quéléver, L. L. J., Rissanen, M. P., Rose, C., Sarnela, N., Schallhart, S., Schuchmann, S., Sengupta, K., Simon, M., Sipilä, M., Tauber, C., Tomé, A., Tröstl, J., Väisänen, O., Vogel, A. L., Volkamer, R., Wagner, A. C., Wang, M., Weitz, L., Wimmer, D., Ye, P., Ylisirniö, A., Zha, Q., Carslaw, K. S., Curtius, J., Donahue, N. M., Flagan, R. C.,

Hansel, A., Riipinen, I., Virtanen, A., Winkler, P. M., Baltensperger, U., Kulmala, M., and Worsnop, D. R.: Multicomponent new particle formation from sulfuric acid, ammonia, and biogenic vapors, Sci. Adv., https://doi.org/10.1126/sciadv.aau5363, 2018.

Leng, C., Zhang, Q., Tao, J., Zhang, H., Zhang, D., Xu, C., Li, X., Kong, L., Cheng, T., Zhang, R., Yang, X., Chen, J., Qiao, L., Lou, S., Wang, H., and Chen, C.: Impacts of new particle formation on aerosol cloud condensation nuclei (CCN) activity in shanghai: case study, Atmos. Chem. Phys., 14, 11353–11365, https://doi.org/10.5194/acp-14-11353-2014, 2014.

Liu, H. J., Zhao, C. S., Nekat, B., Ma, N., Wiedensohler, A., van Pinxteren, D., Spindler, G., Müller, K., and Herrmann, H.: Aerosol hygroscopicity derived from size-segregated chemical composition and its parameterization in the north China plain, Atmos. Chem. Phys., 14, 2525–2539, https://doi.org/10.5194/acp-14-2525-2014, 2014.

Liu, P. F., Zhao, C. S., Göbel, T., Hallbauer, E., Nowak, A., Ran, L., Xu, W. Y., Deng, Z. Z., Ma, N., Mildenberger, K., Henning, S., Stratmann, F., and Wiedensohler, A.: Hygroscopic properties of aerosol particles at high relative humidity and their diurnal variations in the North China Plain, Atmos. Chem. Phys., 11, 3479–3494, https://doi.org/10.5194/acp-11-3479-2011, 2011.

Lv, G., Sui, X., Chen, J., Jayaratne, R., and Mellouki, A.: Investigation of new particle formation at the summit of Mt. Tai, China, Atmos. Chem. Phys., 18, 2243–2258, https://doi.org/10.5194/acp-18-2243-2018, 2018.

McMurry, P. H. and Friedlander, S. K.: New particle formation in the presence of an aerosol, Atmos. Environ. (1967), 13, 1635–1651, https://doi.org/10.1016/0004-6981(79)90322-6, 1979.

Petters, M. D. and Kreidenweis, S. M.: A single parameter representation of hygroscopic growth and cloud condensation nucleus activity, Atmos. Chem. Phys., 7, 1961–1971, https://doi.org/10.5194/acp-7-1961-2007, 2007.

Ren, J., Chen, L., Fan, T., Liu, J., Jiang, S., and Zhang, F.: The NPF Effect on CCN Number Concentrations: A Review and Re-Evaluation of Observations From 35 Sites Worldwide, Geophys. Res. Lett., 48, e2021GL095190, https://doi.org/10.1029/2021GL095190, 2021.

706 Rose, C., Sellegri, K., Moreno, I., Velarde, F., Ramonet, M., Weinhold, K., Krejci, R., Andrade, M.,
707 Wiedensohler, A., Ginot, P., and Laj, P.: CCN production by new particle formation in the free
708 troposphere, Atmos. Chem. Phys., 17, 1529–1541, https://doi.org/10.5194/acp-17-1529-2017, 2017.
709 Rose, D., Gunthe, S. S., Mikhailov, E., Frank, G. P., Dusek, U., Andreae, M. O., and Pöschl, U.:
710 Calibration and measurement uncertainties of a continuous-flow cloud condensation nuclei counter
711 (DMT-CCNC): CCN activation of ammonium sulfate and sodium chloride aerosol particles in theory
712 and experiment, Atmos. Chem. Phys., 8, 1153–1179, https://doi.org/10.5194/acp-8-1153-2008, 2008.
713 Shen, X., Sun, J., Kivekäs, N., Kristensson, A., Zhang, X., Zhang, Y., Zhang, L., Fan, R., Qi, X., Ma, Q.,
714 and Zhou, H.: Spatial distribution and occurrence probability of regional new particle formation events
715 in eastern China, Atmos. Chem. Phys., 18, 587 – 599, https://doi.org/10.5194/acp-18-587-2018, 2018.
716 Sipilä, M., Berndt, T., Petäjä, T., Brus, D., Vanhanen, J., Stratmann, F., Patokoski, J., Mauldin, R. L.,
717 Hyvärinen, A.-P., Lihavainen, H., and Kulmala, M.: The role of sulfuric acid in atmospheric nucleation,
718 Science, 327, 1243–1246, https://doi.org/10.1126/science.1180315, 2010.
719 Sun, Y. L., Wang, Z. F., Du, W., Zhang, Q., Wang, Q. Q., Fu, P. Q., Pan, X. L., Li, J., Jayne, J., and
720 Worsnop, D. R.: Long-term real-time measurements of aerosol particle composition in beijing, china:
721 seasonal variations, meteorological effects, and source analysis, Atmos. Chem. Phys., 15, 10149–10165,
722 https://doi.org/10.5194/acp-15-10149-2015, 2015.
723 Tröstl, J., Chuang, W. K., Gordon, H., Heinritzi, M., Yan, C., Molteni, U., Ahlm, L., Frege, C., Bianchi,
724 F., Wagner, R., Simon, M., Lehtipalo, K., Williamson, C., Craven, J. S., Duplissy, J., Adamov, A.,
725 Almeida, J., Bernhammer, A.-K., Breitenlechner, M., Brilke, S., Dias, A., Ehrhart, S., Flagan, R. C.,
726 Franchin, A., Fuchs, C., Guida, R., Gysel, M., Hansel, A., Hoyle, C. R., Jokinen, T., Junninen, H.,
727 Kangasluoma, J., Keskinen, H., Kim, J., Krapf, M., Kürten, A., Laaksonen, A., Lawler, M., Leiminger,
728 M., Mathot, S., Möhler, O., Nieminen, T., Onnela, A., Petäjä, T., Piel, F. M., Miettinen, P., Rissanen, M.
729 P., Rondo, L., Sarnela, N., Schobesberger, S., Sengupta, K., Sipilä, M., Smith, J. N., Steiner, G., Tomè,
730 A., Virtanen, A., Wagner, A. C., Weingartner, E., Wimmer, D., Winkler, P. M., Ye, P., Carslaw, K. S.,
731 Curtius, J., Dommen, J., Kirkby, J., Kulmala, M., Riipinen, I., Worsnop, D. R., Donahue, N. M., and
732 Baltensperger, U.: The role of low-volatility organic compounds in initial particle growth in the
733 atmosphere, Nature, 533, 527–531, https://doi.org/10.1038/nature18271, 2016.

Wang, H., Zhu, B., Shen, L., An, J., Yin, Y., and Kang, H.: Number size distribution of aerosols at Mt. Huang and nanjing in the Yangtze River delta, china: effects of air masses and characteristics of new particle formation, Atmos. Res., 150, 42–56, https://doi.org/10.1016/j.atmosres.2014.07.020, 2014.

Wang, Z. B., Hu, M., Yue, D. L., Zheng, J., Zhang, R. Y., Wiedensohler, A., Wu, Z. J., Nieminen, T., and Boy, M.: Evaluation on the role of sulfuric acid in the mechanisms of new particle formation for beijing case, Atmos. Chem. Phys., 11, 12663–12671, https://doi.org/10.5194/acp-11-12663-2011, 2011.

Wildt, J., Mentel, T. F., Kiendler-Scharr, A., Hoffmann, T., Andres, S., Ehn, M., Kleist, E., Müsgen, P., Rohrer, F., Rudich, Y., Springer, M., Tillmann, R., and Wahner, A.: Suppression of new particle formation from monoterpene oxidation by NOx, Atmos. Chem. Phys., 14, 2789–2804, https://doi.org/10.5194/acp-14-2789-2014, 2014.

Williamson, C. J., Kupc, A., Axisa, D., Bilsback, K. R., Bui, T., Campuzano-Jost, P., Dollner, M., Froyd, K. D., Hodshire, A. L., Jimenez, J. L., Kodros, J. K., Luo, G., Murphy, D. M., Nault, B. A., Ray, E. A., Weinzierl, B., Wilson, J. C., Yu, F., Yu, P., Pierce, J. R., and Brock, C. A.: A large source of cloud condensation nuclei from new particle formation in the tropics, Nature, 574, 399–403, https://doi.org/10.1038/s41586-019-1638-9, 2019.

Wu, C. and Yu, J. Z.: Determination of primary combustion source organic carbon-to-elemental carbon (OC / EC) ratio using ambient OC and EC measurements: secondary OC-EC correlation minimization method, Atmos. Chem. Phys., 16, 5453–5465, https://doi.org/10.5194/acp-16-5453-2016, 2016.

Wu, Z. J., Zheng, J., Shang, D. J., Du, Z. F., Wu, Y. S., Zeng, L. M., Wiedensohler, A., and Hu, M.: Particle hygroscopicity and its link to chemical composition in the urban atmosphere of Beijing, china, during summertime, Atmos. Chem. Phys., 16, 1123–1138, https://doi.org/10.5194/acp-16-1123-2016, 2016.

Xiao, S., Wang, M. Y., Yao, L., Kulmala, M., Zhou, B., Yang, X., Chen, J. M., Wang, D. F., Fu, Q. Y., Worsnop, D. R., and Wang, L.: Strong atmospheric new particle formation in winter in urban shanghai, china, Atmos. Chem. Phys., 15, 1769–1781, https://doi.org/10.5194/acp-15-1769-2015, 2015.

Xu, W., Ovadnevaite, J., Fossum, K. N., Lin, C., Huang, R.-J., O'Dowd, C., and Ceburnis, D.: Aerosol hygroscopicity and its link to chemical composition in the coastal atmosphere of Mace Head: marine and

761 continental air masses, Atmos. Chem. Phys., 20, 3777–3791, https://doi.org/10.5194/acp-20-3777-2020,
762 2020.
763 Yao, L., Garmash, O., Bianchi, F., Zheng, J., Yan, C., Kontkanen, J., Junninen, H., Mazon, S. B., Ehn,
764 M., Paasonen, P., Sipilä, M., Wang, M., Wang, X., Xiao, S., Chen, H., Lu, Y., Zhang, B., Wang, D., Fu,
765 Q., Geng, F., Li, L., Wang, H., Qiao, L., Yang, X., Chen, J., Kerminen, V.-M., Petäjä, T., Worsnop, D.
766 R., Kulmala, M., and Wang, L.: Atmospheric new particle formation from sulfuric acid and amines in a
767 chinese megacity, Science, https://doi.org/10.1126/science.aao4839, 2018.
768 Yli-Juuti, T., Nieminen, T., Hirsikko, A., Aalto, P. P., Asmi, E., Hõrrak, U., Manninen, H. E., Patokoski,
769 J., Dal Maso, M., Petäjä, T., Rinne, J., Kulmala, M., and Riipinen, I.: Growth rates of nucleation mode
770 particles in hyytiälä during 2003&minus- 2009: variation with particle size, season, data analysis method
771 and ambient conditions, Atmos. Chem. Phys., 11, 12865–12886, https://doi.org/10.5194/acp-11-12865-
772 2011, 2011.
773 Yu, F., Luo, G., Nadykto, A. B., and Herb, J.: Impact of temperature dependence on the possible
774 contribution of organics to new particle formation in the atmosphere, Atmos. Chem. Phys., 17, 4997–
775 5005, https://doi.org/10.5194/acp-17-4997-2017, 2017.
776 Yue, D. L., Hu, M., Zhang, R. Y., Wu, Z. J., Su, H., Wang, Z. B., Peng, J. F., He, L. Y., Huang, X. F.,
777 Gong, Y. G., and Wiedensohler, A.: Potential contribution of new particle formation to cloud
778 condensation nuclei in Beijing, Atmos. Environ., 45, 6070–6077,
779 https://doi.org/10.1016/j.atmosenv.2011.07.037, 2011.
780 Yue, G. K. and Hamill, P.: The homogeneous nucleation rates of H2SO4-H2O aerosol particles in air, J.
781 Aerosol Sci., 10, 609–614, https://doi.org/10.1016/0021-8502(79)90023-5, 1979.
782 Zaveri, R. A., Wang, J., Fan, J., Zhang, Y., Shilling, J. E., Zelenyuk, A., Mei, F., Newsom, R., Pekour,
783 M., Tomlinson, J., Comstock, J. M., Shrivastava, M., Fortner, E., Machado, L. A. T., Artaxo, P., and
784 Martin, S. T.: Rapid growth of anthropogenic organic nanoparticles greatly alters cloud life cycle in the
785 Amazon rainforest, Science Advances, 8, eabj0329, https://doi.org/10.1126/sciadv.abj0329, 2022.
786 Zhan, Y., Xie, M., Gao, D., Wang, T., Zhang, M., and An, F.: Characterization and source analysis of
787 water-soluble inorganic ionic species in PM2.5 during a wintertime particle pollution episode in Nanjing,
788 china, Atmos. Res., 262, 105769, https://doi.org/10.1016/j.atmosres.2021.105769, 2021.

789 Zhu, W., Shang, S., Wang, J., Wu, Y., Deng, Z., Ran, L., Kuang, Y., Tang, G., Huang, X., Pan, X., Liu,
790 L., Xu, W., Sun, Y., Hu, B., Wang, Z., and Liu, Z.: Oxidation-driven acceleration of NPF-to-CCN
791 conversion under polluted atmosphere: evidence from mountain-top observations in Yangtze River delta,
792 Atmos. Chem. Phys., 26, 1947–1965, https://doi.org/10.5194/acp-26-1947-2026, 2026